Turkish Journal of Electrical Engineering & Computer Sciences

http://journals.tubitak.gov.tr/elektrik/

Research Article

Turk J Elec Eng & Comp Sci
(2016) 24: 3123 – 3143

doi:10.3906/elk-1406-14

# Protection of a multiterminal DC compact node feeding electric vehicles on electric railway systems, secondary distribution networks, and PV systems

**Jesus Casa HERNANDEZ*, Francisco Sanchez SUTIL, Pedro Gomez VIDAL**
Deptartment of Electrical Engineering, University of Jaén, Campus de las Lagunillas, Jaén, Spain

**Received:** 06.06.2014 • **Accepted/Published Online:** 10.03.2015 • **Final Version:** 15.04.2016

**Abstract:** This paper describes a multiterminal DC compact node consisting of voltage-source converters and DC-DC converters as a promising arrangement to feed electric vehicle (EV) charging stations with renewable power sources. This research analyzed the behavior of the node currents under DC faults, and more specifically their natural response, which can produce challenging electrical protection requirements. An electrical protection system was thus designed based on the use of protective devices that included protective relays, solid state circuit breakers and hybrid circuit breakers. These protective devices monitor local readings to detect and isolate DC faults as quickly as possible. This highlighted the fact that there are devices, available on the market, that comply with the fast response requirement to prevent damage or destruction of the converters and filter capacitors of the node.

**Key words:** DC power systems, voltage-source converter, power system protection, fault current, solid-state switch

## 1. Introduction

Electrical vehicles (EVs) reduce $CO_2$ emissions generated by the transportation sector. However, their large-scale use is not without problems since it involves a massive implantation of EV charging stations in conventional secondary distribution networks (SDNs) [1]. Furthermore, it is expected that this implantation will eventually include the two main categories of railway traction systems (RTSs): the AC and DC systems [2–4].

This paper proposes a new paradigm for the feeding of EV charging stations from a DC reference node. This low-voltage DC compact node connects a 0.4-kV AC SDN, a 25-kV AC RTS, a 3-kV DC RTS, reversible EV charging stations (i.e. power to/from the grid [V2G]), and a local distributed generation (DG) system by means of voltage-source converters (VSCs) and DC-DC converters (DC-DCCs). The DG includes both a photovoltaic (PV) system and backup storage systems (battery and supercapacitor [SC]). This new arrangement brings mutual benefits derived from the inclusion of two intermittent renewable power sources in the EV charging stations: PV power and regenerative braking power in RTSs.

Rather than an analysis of control strategies used, because of space limitations the main focus of this research was to identify characteristic behaviors of DC-DCC-based and VSC-based compact node currents under DC faults and to design the hardware in the resulting protection system. The work reported in [5] focused on the elaboration of a unified set of requirements for grid-interconnection of bidirectional EV charging stations to distribution networks and RTSs. This included the definition of required protection relays and their settings. This paper goes a step further by describing the hardware in the protection system (measurement equipment,

*Correspondence: jcasa@ujaen.es

protective devices, and relays) as well as its feasibility. This feasibility involves verifying the operating capacity of hardware available on the market and its effectiveness. Operating capacity means that the settings of the protection system designed must be in accordance with the variation of its control variable under different types of DC faults in the node. Effectiveness implies that the faults are eliminated within the specified response time to prevent damage or destruction of the converters and filter capacitors of the node.

DC fault currents in compact nodes pose many challenges that demand advanced electrical protection requirements. These challenges include the following: 1) protection against currents of high magnitude and rate of change; 2) prevention of significant voltage transients when operating protective devices; 3) choice of DC circuit-breaker technologies so that protective devices can operate at the required speed; 4) low fault withstand rating of the converter; and 5) lack of standards, guidelines, and experience [6]. Furthermore, the development of an effective multiterminal node concept can contribute to the increase of sensors and communication infrastructure [7].

Section 2 of this paper describes the architecture of a multiterminal DC compact node. The design of the electrical protection system of the node is outlined in Section 3. Section 4 explains the theoretical premises underlying the current response for different DC faults with particular emphasis on how transient current behavior affects electrical protection requirements. Finally, Section 5 presents the dynamic performance of the protection system in the multiterminal DC compact node that feeds EV charging stations.

As part of this research, models of the converters and control strategies that form the node were implemented with Matlab/Simulink. In addition, protective devices, filter capacitances, resistances, and inductances between converters and fault points were also taken into account.

## 2. Basic layout of the multiterminal DC compact node

Because the interfacing system needs to be multiterminal, VSCs and DC-DCCs are used to link different sources and loads by means of a DC bus [6,8]. VSCs interface the AC/DC RTS, SDN, and the AC V2G charging station to a 750-V DC bus (Figure 1). Furthermore, the node employs DC-DCCs to connect the DC sources (battery and SC bank, DC PV system, and DC V2G charging station). All converters use capacitive filters, and linking feeder lengths range from 5 to 10 m.

For safety reasons, galvanic isolation is required in RTSs and SDNs [9,10]. Thus, this galvanic isolation is provided between the DC bus and the DC RTS or the AC SDN by adding an interconnection transformer with a unity ratio before the VSC. There is also a transformer between the AC RTS and the DC bus. The three-phase (single-phase) VSCs use pulse width modulation (PWM) to control the VSC output voltage, and hence, the voltages across the grid (generation source) filter. This means that the current going through the filter can be controlled and the power flows between the grid (SDN or AC/DC RTS) and the VSC [11]. The power flow can be bidirectional, and active and reactive power can be individually controlled [12].

The VSC current control system adopted uses a vector controller implemented in the synchronous DQ-coordinate system, where the positive sequence AC components appear as DC quantities [13]. The DC-DCCs use pulse width modulation (PWM) that controls the DC-DCC output voltage, and hence, the voltages throughout the output (generation source) filter. This means that the bidirectional power flow between the DC bus and the generation source can be controlled. PV renewable power has no bidirectional power flow. The power management strategy is geared to controlling the power from different generation sources so that the bidirectional load demand (AC and DC V2G charging stations) can be satisfied with the least possible cost, while giving the highest priority to PV power and regenerative braking power in RTSs.

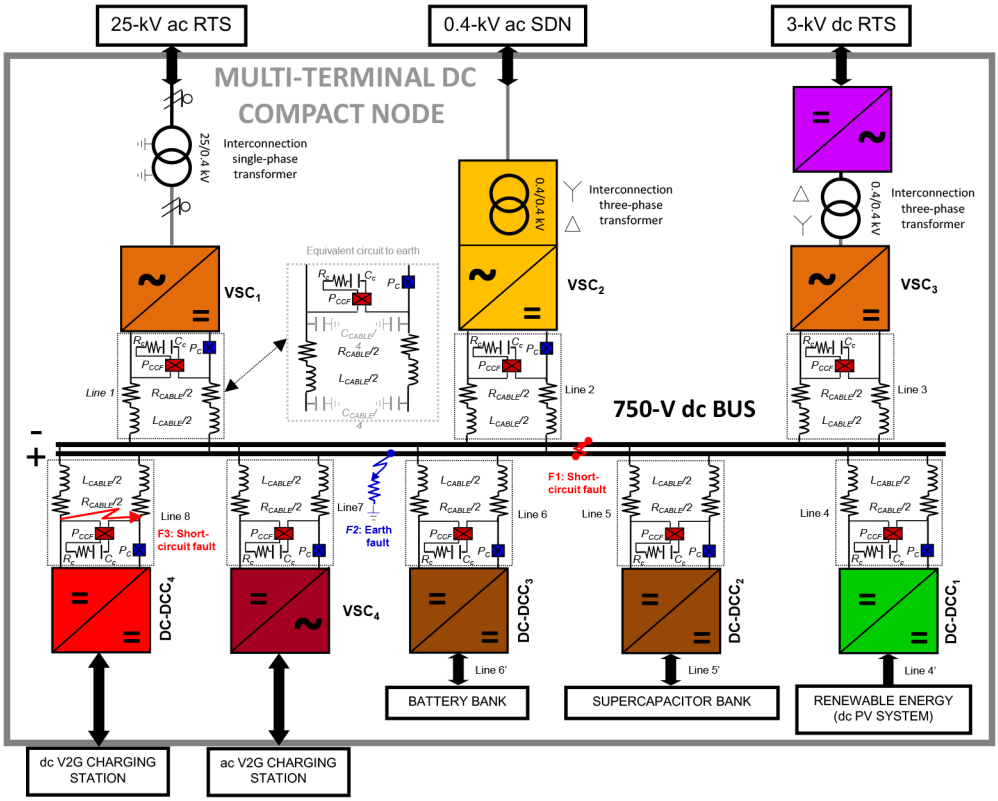


**Figure 1.** Block diagram of the multiterminal DC compact node.

## 3. Electrical protection of the multiterminal DC compact node

The fault current withstand of VSCs and DC-DCCs is much lower than that of thyristor-based converters [6,14]. Therefore, the protection system design of traditional high-voltage DC distribution systems (thyristor converter-based systems) [15–17] cannot be applied to multiterminal DC compact nodes. In addition, short-circuit currents in high-voltage or low-voltage DC distribution systems are regulated by means of the large smoothing reactance of cables. Consequently, the DC faults in DC compact nodes must be limited and interrupted much faster than in DC distribution systems.

Many references report the short-circuit current behavior for converter-based low-voltage systems [6,7,18–24], the behavior of insulated-gate bipolar transistors (IGBTs) in fault conditions [25,26], the protection techniques for low-voltage (high-voltage) DC distribution systems [6,20–24,27], and DC compact systems (nodes) [6,7]. However, the dynamic performance of the electrical protection system in DC compact systems with solid state circuit breakers (SSCBs), hybrid circuit breakers (HCBs), and protective relays, especially during operation, has not been assessed in any depth. This is of great interest for the node analyzed since it involves different types of VSCs (three-phase and single-phase converters) and DC-DCCs, as well as sources of different characteristics (0.4-kV AC SDN, 25-kV AC RTS, 3-kV DC RTS, DC PV system, battery and SC banks, and VE battery).

Until now the assessment of the dynamic performance of protection systems has only been evaluated in studies of high-voltage DC applications, such as electric ships and high-voltage DC distribution systems [14,28]. Although Salomonsson et al. [6] assessed dynamic performance in this context, their research was limited to the

use of fast DC fuses in a three-phase converter connected to an AC SDN. Therefore, a protection system for a DC compact node was initially designed, based on the use of SSCBs, HCBs, and protective relays. An evaluation was then carried out of the dynamic performance of the protection system designed under DC faults. Current and voltage transients were subsequently identified and quantified to illustrate the impact of the performance of the protection system.

### 3.1. Protection options

The common practice for protecting low-voltage DC compact systems is to install protection on the DC side and to shut down the converter in case of DC faults [6,7]. Nonetheless, the rate of current change can be so rapid that the converter current control is unable to detect the fault in time, which results in a failure of the solid-state switches of the converter (e.g., IGBT). The control time step cannot be longer than the short-circuit current rise time. IGBT manufacturers define its maximum overcurrent capability to be 2–3 times the nominal current during various milliseconds [14,22]. Furthermore, when the coordination of various protective devices in series is required, a protection scheme based on unit protection is advisable [7,21,24].

However, in low-voltage DC distribution systems, converters are required to inject short-circuit current that enables the fast operation of the protective devices [22,23] as a way to ensure minimum disruption of supply to the loads. Converters need to handle the short-circuit current by means of a suitable control scheme [22].

### 3.2. Protection system design

The protection system designed for the multiterminal DC compact node must detect and isolate DC faults as quickly as possible. This system consists of measurement equipment, protective devices, and relays ( $P_C$ and $P_{CCF}$ protection in Figure 1).

Overcurrent protective devices commercially available for low-voltage DC systems (apart from fuses) are SSCBs, HCBs, and electro mechanical circuit breakers (EMCBs). In addition, protective relays can use information from measured voltages and currents to calculate time derivatives [29] and the step changes of currents/voltages in order to determine whether a fault has occurred.

Because of the limitations of fuses and EMCBs (long breaker operation times, e.g., fuses $\sim$ 2 ms, EMCB $\sim$ 4–500 ms [8]), SSCBs and HCBs have become valid options for protecting DC systems. For this reason, the protection prototype designed in this research uses these protective devices. A semiconductor-based bidirectional switch (bidirectional SSCB, Figure 2) was designed to protect each converter capacitive filter ( $P_{CCF}$ protection in Figure 1). The DC node protection is based on fast converter shutdown since it is difficult to isolate DC faults in compact nodes. Nonetheless, the converter needs to be protected against DC faults by additional converter protection (bidirectional HCB, Figure 3), which is located externally ( $P_C$ protection in Figure 1).

#### 3.2.1. Solid state circuit breaker

SSCBs use solid-state switches [IGBT, a gate turn-off thyristor (GTO), an integrated gate-commutated thyristor (IGCT), and an emitter turn-off thyristor (ETO)] to provide the power switching. The electrical utility industry is already using ETO-based [30] and IGCT-based SSCBs [31]. Market research for power devices shows that the IGCT is the best option. IGCT-based SSCBs have a high current capacity and a switching speed of about 11 *mu* s. IGBT-based SSCBs are not frequently used because of their lower current capacity and higher on-state losses despite their higher switching speed (about six times greater). Nonetheless, a lower turn-off speed has the advantage of a bus voltage with lower ringing frequency during fault interruptions.

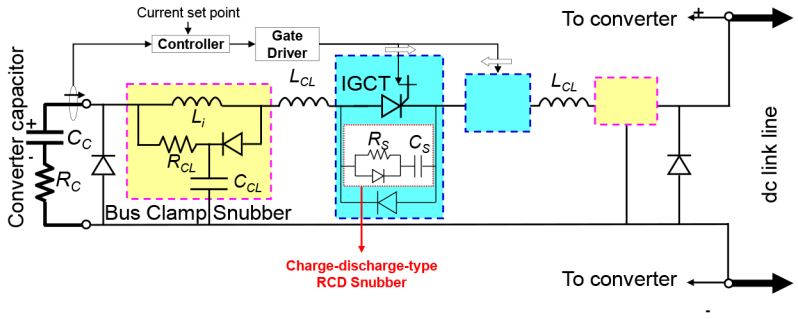


**Figure 2.** Diagram of the $P_{CCF}$ protection: bidirectional IGCT-based SSCB.

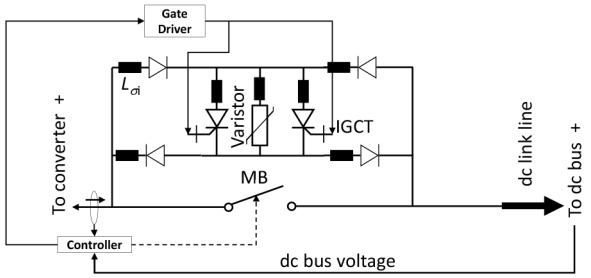


**Figure 3.** Diagram of the $P_C$ protection: bidirectional HCB.

Figure 2 shows the diagram of the $P_{CCF}$ protection proposed in this research to protect converter capacitive filters. It consists of bidirectional IGCT-based SSCB with snubber circuits, relays, and measurement equipment. The snubber circuit protects SSCB from high voltage transients because of the inductance of the bus cable [11,32]. The trip signal is triggered when the current relay exceeds a given threshold.

### 3.2.2. Hybrid circuit breaker

Although the SSCB solution is able to break currents in the kA range within a few $mu$ s, it has higher on-state losses than mechanical breakers (MBs). Therefore, Figure 3 shows the combination of an MB and an active turn-off semiconductor switch [33,34], which was used in this research to externally protect the converter ( $P_C$ protection in Figure 1). This permits a millisecond fault interruption by using a contact gap required in a low-voltage system [35]. The trip signal is triggered when the current relay exceeds a given threshold and the bus voltage relay dips below a certain threshold.

## 4. Analysis of the DC fault current response in the multiterminal DC compact node

This section presents the analytical expressions that describe the typical fault current response in the multiterminal DC node. The types of faults analyzed were short-circuit and line-to-earth faults.

### 4.1. DC short-circuit fault

For compact DC systems, the discharge of the filter capacitor throughout the system usually dominates the fault current profile immediately following DC fault (natural response). Meanwhile the contribution from the converter-interfaced generation source forms the latter part of the response (forced response) [6,7,14,18,21]. Nonetheless, the current profile changes, depending on the source of characteristic impedance, filter size, configuration, and converter and generation technologies used.

The short-circuit fault can be represented for each $i$th VSC$_i$ (DC-DCC$_i$) of the multiterminal DC node by the equivalent circuits in Figures 4a, 4b, and 4c. In these circuits, $R$ represents the line resistance of both cables from each $i$th VSC$_i$ (DC-DCC$_i$) to the fault point, whereas $R_c$ ($R' = R + R_c$) designates the equivalent series resistance of the converter filter capacitance $C_c$. The inductor $L$ represents the total line inductance of both cables.

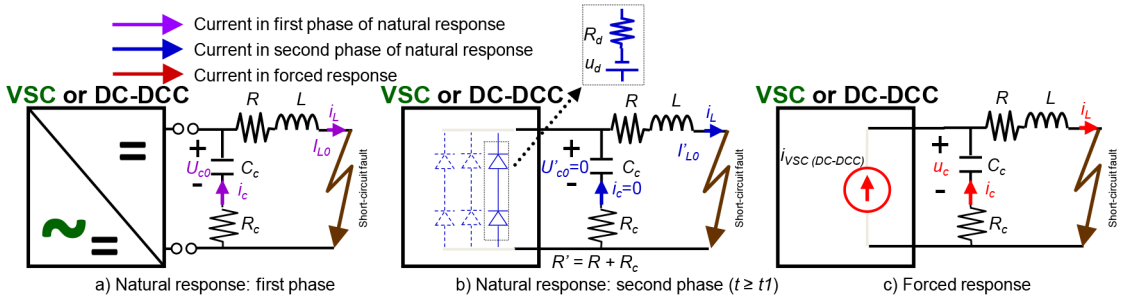


**Figure 4.** Equivalent circuits for each $i$th VSC$_i$ (DC-DCC$_i$) in the case of a DC short-circuit fault in the node.

### 4.1.1. Natural response: first phase (after the fault)

Although the natural response of the fault current can be described by considering an equivalent $RLC$ circuit (Figures 4a and 4b), its analysis is performed in two separate phases [6,7]. In the first phase, the capacitor $C_c$, precharged to the initial voltage $U_{c0}$, discharges through the resistance and inductance (Figure 4a). This discharge is shown for each converter of the multiterminal DC compact node in Figures 5 to 8. The current in the Laplace domain is given in the following expression:

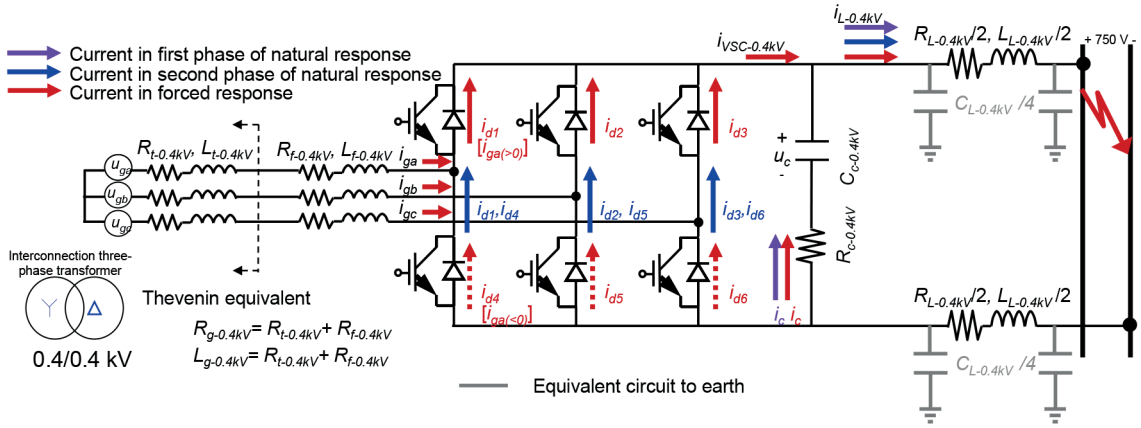


**Figure 5.** VSC between the DC bus and 0.4-kV AC SDN with a DC short-circuit fault.

$$i_L(s) = U_{cO}/L + I_{LO}s\frac{U_{cO}/L + I_{LO}s}{s^2 + (R'/L)s + (1/LC_c)} \tag{1}$$

where $I_{L0}$ is the initial current through the inductor $L$, set according to prefault operation. Since the converter-side current is negligible for the period immediately after the fault [6,7], the VSC (DC-DCC) can be disconnected from the $RLC$ circuit. The current response is the sum of two decreasing exponential terms:

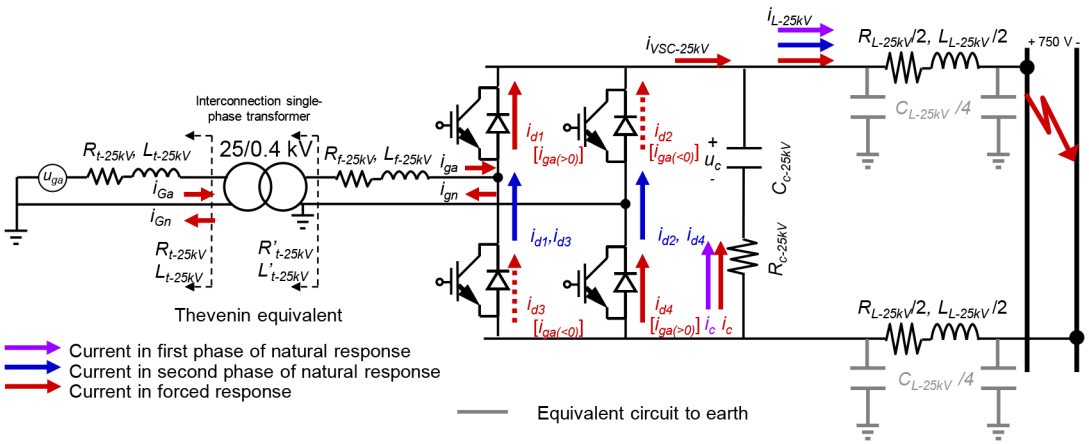


**Figure 6.** VSC between the DC bus and 25-kV AC RTS with a DC short-circuit fault.

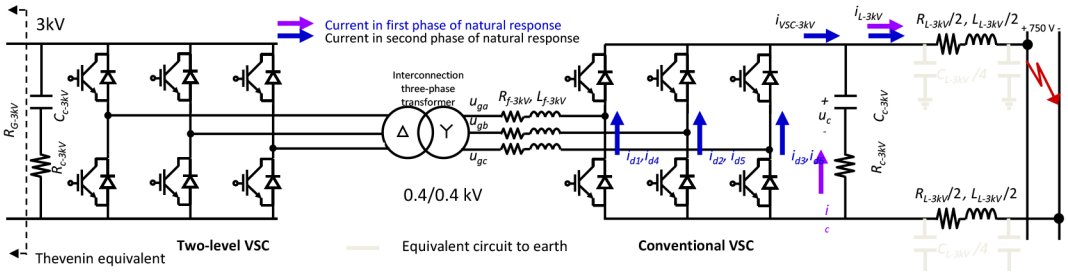


**Figure 7.** VSCs between the DC bus and 3-kV DC RTS with a DC short-circuit fault.

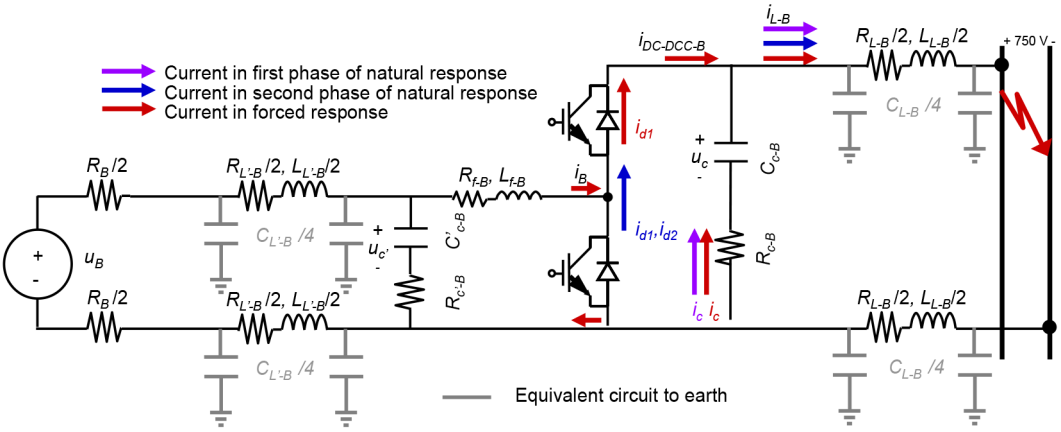


**Figure 8.** DC-DCC between the DC bus and battery bank (generation source) with a DC short-circuit fault.

$$i_L(t) = 1A_1e^{s_1t} + A_2e^{s_2t} \tag{2}$$

where $A_{1,2}$ are coefficients that depend on initial conditions, and $s_{1,2}$ are the roots of the following equation:

$$s_{1,2} = \alpha^2 - \omega_0^2 - \alpha \pm \sqrt{\alpha^2 - \omega_0^2} \tag{3}$$

where $\alpha = R' / (2\times\ L)$ is the exponential damping coefficient and $\omega_0 = 1 / \sqrt{(LC_c)}$ is the resonant frequency of the circuit.

The location of the roots in Eq. (3), as a function of the relative magnitudes of $\alpha^2$ and $\omega_0^2$, determines the form of the current response, where $\alpha^2 > \omega_0^2, \alpha^2 = \omega_0^2$, $\alpha^2 < \omega_0^2$ represent over-, critically, and underdamped fault responses, respectively. For underdamped systems, the current response is oscillatory. When the Euler identity is applied to Eq. (2) and the terms are substituted for the initial conditions, the underdamped current response is set by:

$$i_L(t) U_{c0} \frac{U_{c0}}{L\omega_d} e^{-\alpha t} \sin(\omega_d t) L0 I_{L0} e^{-\alpha t} [\cos(\omega_d t) - \frac{\alpha}{\omega_d} \sin(\omega_d t)] \tag{4}$$

where $\omega_d$ is the damped resonant frequency:

$$\omega_d = \sqrt{\omega_0^2 - \alpha^2} \tag{5}$$

Because of the large converter filter capacitance and relatively low cable inductance (short cable lengths), the dominant part of any underdamped fault current in Eq. (4) is due to the initial voltage across the converter filter capacitance. Thus, the term of the initial inductor current $I_{L0}$ can be regarded as negligible [7]. Furthermore, for highly underdamped conditions ($\alpha^2 << \omega_0^2$), $\omega_d$ tends to $\omega_0$, and Eq. (4) may be reduced as follows:

$$i_L(t) = \frac{U_{c0}}{\sqrt{L/C_c}} e^{-\alpha t} \sin(\omega_0 t) \tag{6}$$

The time taken for the current to reach its peak magnitude can be obtained from Eq. (6) by equating its derivative to zero. Generally speaking, in DC compact electrical systems, this time is very short [6,7,14,21]. Its value for highly underdamped conditions is given in the following expression:

$$t_{peak} \simeq 0(1/\omega_0) \arctan(\omega_0/\alpha) \tag{7}$$

However, with high-impedance faults, an overdamped response can develop. The current and peak time equations are:

$$i_L(t) = U_{c0} \frac{U_{c0}}{L(s_1 - s_2)\omega_d} \left(e^{s_1 t} - e^{s_2 t}\right) \tag{8}$$

$$t_{peak} = 2\ln(s_2/s_1)/(s_2 - s_1) \tag{9}$$

#### 4.1.2. Natural response: second phase (freewheeling phase)

After the occurrence of the peak current, $L--C$ oscillations in the circuit converter-line can cause the voltage for the filter capacitance of VSCs (DC-DCCs) to become negative [6,7,21]. This has the effect of reversing the voltage at the converter terminals. When this voltage is sufficiently high, it causes the conducting of the converter freewheeling diodes. Thus, there is an alternative current path, regardless of the state of the active switching devices within the converter, and this changes the response of the circuit converter-line (Figure 4b).

In this phase ($t > t_1$, where $t_1$ is the time at which the capacitor voltage reaches zero) $u_d$ and $R_d$ are the sum of the on-state voltages and resistances of the diodes in any converter leg. This second phase of the discharge of the cable inductor is modelled by a first-order equivalent circuit (Figures 4b), where the inductor current circulates through the on-state freewheeling diodes of the converter. The inductor current is:

$$i_L(t) = L0 I'_{L0} e^{-(R/L)t} \tag{10}$$

where $I_{L0}^{'}$ is the initial inductor current for $t = t_1$. Depending on the converter in the multiterminal DC compact node (three-phase or single-phase VSC or DC-DCC), the inductor current circulates through the following couples of freewheeling diodes of the converter: 1) $d_1/d_4$, $d_2/d_5$, and $d_3/d_6$ in the three-phase VSC of the 0.4-kV AC SDN (Figure 5); 2) $d_1/d_3$ and $d_2/d_4$ in the single-phase VSC of the 25-kV AC RTS (Figure 6); 3) $d_1/d_4$, $d_2/d_5$, and $d_3/d_6$ in the VSC of the 3-kV DC RTS (Figure 7); and 4) $d_1/d_2$ in the DC-DCC of the battery bank (Figure 8).

The freewheeling diodes of the converter carry one third, half, or all of the inductor discharge current for the above-mentioned cases. This is the most challenging phase for these freewheeling diodes since the freewheeling overcurrent is very abrupt with a high initial value, which can immediately damage the diodes.

#### 4.1.3. Forced response: current feeding phase from the grid or generation source

The forced response is the DC-link of the capacitor and cable inductor under a forced current source response ($i_{VSC}$ [$i_{DC-DCC}$]). When the control of the VSC or DC-DCC is blocked, $u_C$ is not necessarily zero (Figure 4c).

To calculate the fault current contribution from the three-phase VSC of the 0.4-kV AC SDN (Figures 4c and 5), the three-phase short-circuit current is obtained by three-phase short-circuit analysis. When the grid voltage for phase $a$ after the fault occurs is $u_{ga} = U_g \sin(\omega_s t + \beta)$, with $U_g$ being the amplitude, $\omega_s$ the synchronous frequency, and $\beta$ the voltage angle at $t_1$, the phase current is:

$$i_{ga}(t) = gI_g \sin(\omega_s t + \beta - \varphi) + [I_{g0} \sin(\beta - \varphi_0) - I_g \sin(\beta - \varphi)]e^{-\alpha/\tau} \tag{11}$$

where $\tau = (L_{g-0.4kV} + L_{L-0.4kV}) / (R_{g-0.4kV} + R_{L-0.4kV})$, $\varphi = \arctan(\omega_s \tau)$, $I_{g0}$, and $\varphi_0$ are the initial grid current amplitude and phase angle, respectively. The positive $i_{ga}$ current flows from diode $d_1$ to contribute to $i_{VSC-0.4kV}$, with those of $i_{gb}$ and $i_{gc.}$ Accordingly, the total $i_{VSC-0.4kV}$ is the positive three-phase short-circuit current summation:

$$i_{_{VSC-0.4kV}}(t)d_1 i_{d_1}(t)d_2 i_{d_2}(t)d_3 i_{d_3} = t)ga, (>0)i_{ga,(>0)}(t)gb, (>0)i_{gb,(>0)}(t)gc, (>0)i_{gc,(>0)}(t) \tag{12}$$

and the inductor current is:

$$i_{_{L-0.4kV}}(t)sA\sin(\omega_s t + \gamma) - t/\tau Be^{-t/\tau}1C_1(\omega_0/\omega_d)e^{-\alpha t}\sin(\omega_d t + \varepsilon)2(C_2/\omega_d)e^{-\alpha t}\sin(\omega_d t) \tag{13}$$

where $A = I_g[(1 - \omega_s^2 \times L_{L-0.4kV} \times C_{c-0.4kV})^2 + (R_{L-0.4kV} \times C_{c-0.4kV})^2]^{-(1/2)}$, $\gamma = \beta - \varphi - \theta$, $\theta = \arctan[R_{L-0.4kV} \times C_{c-0.4kV} / (1 - \omega_s^2 \times L_{L-0.4kV} \times C_{c-0.4kV})]$, $\varepsilon = \arctan(\omega_d / \alpha)$, $B = I_g[\tau^2 / (\tau^2 - \tau \times R_{L-0.4kV} \times C_{c-0.4kV} + L_{L-0.4kV} \times C_{c-0.4kV})]$, $C_1 = -(A \times \sin\gamma + B)$, and $C_2 = B / \tau + \omega_s \times A\cos\gamma$. The negative currents $i_{ga}$, $i_{gb,}$ and $i_{gc}$ flow through diodes $d_4$, $d_{5,}$ and $d_6$, respectively.

To calculate the fault current contribution from the single-phase VSC of the 25-kV ac RTS (Figures 4c and 6), the two converter semilegs with on-state diodes need to be taken into account. Therefore, the $i_{VSC-25kV}$ current is the result of the positive $i_{ga}$ current from diodes $d_1/d_4$ and the negative $i_{ga}$ current from diodes $d_2/d_3$. For this reason, the $i_{VSC-25kV}$ expression has the same pattern as Eq. (12). Nonetheless, the interconnection impedance of the single-phase transformer should also be considered.

To calculate the fault current contribution from 3-kV DC RTS, it should be highlighted that the configuration of the VSCs between the DC bus and 3-kV DC RTS avoids the injection of 3-kV DC grid-side current into the DC fault (Figure 7). Therefore, Eqs. (12) and (13) are not applicable.

To calculate the fault current contribution from the DC-DCC of the battery bank (Figures 4c and 8), it is only necessary to focus on the semileg of the converter with the on-state diode ($d_1$).

### 4.2. DC earth fault

There are different approaches to the design of earthing systems in electric power systems. Evidently, different solutions result in different performances [36]. Earthing is used for the detection of earth faults and for personnel and equipment safety [37]. The DC compact node can be earthed or unearthed. Although in the past the earthed configuration permitted easier fault detection [23], new protective devices in unearthed configurations (insulation monitoring devices) [38] make this detection even easier. Therefore, an unearthed configuration was chosen for this node since it is the safest configuration for protection against electric shock [38].

Within this configuration, the DC compact node only includes the neutral point of the step-down transformer in the link of the 25-kV AC RTS as the earthing point. An earth fault forms an earth loop with this earthing point, and it is only the blocked single-phase VSC of the 25-kV AC RTS that feeds the grid-side current as an uncontrolled rectifier with the DC bus voltage modified to the rectified voltage. This means that the current flows through diode $d_1$ (Figure 9). However, fault resistance $R_f$ cannot be ignored in this case since earth fault resistance can amount to hundreds of ohms [6,39].

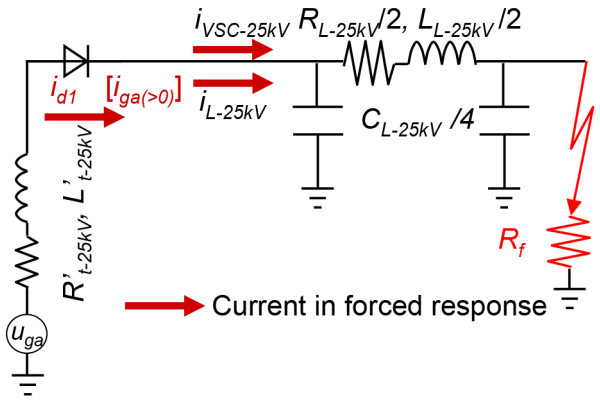


**Figure 9.** Equivalent circuit for the single-phase VSC between the DC bus and the 25-kV AC RTS with a DC earth fault.

## 5. Case study

This section assesses the dynamic performance of the protection system (protective devices) of the multiterminal DC compact node under DC faults. The primary concerns are short-circuit (*F1* and *F3*) and line-to-earth (*F2*) faults since these conditions are the most severe for the reversible VSCs and DC-DCCs.

Both types of faults were performed at one arbitrary operating point of the DC node (the one shown in the Table). In what follows, the beginning of the fault is referred to in graphs as zero time. The analysis was carried out by Matlab/Simulink simulations. The Table shows the characteristics of the parameters used in the simulations for the multiterminal DC node. In addition, the node has storage systems consisting of a 55 Ah Li-ion battery bank and a SC bank with a total capacity of 15.95 F. The maximum short-circuit current accounted at the 0.4-kV AC SDN and 3-kV DC RTS was 50 kA; it was 15 kA for the 25-kV AC RTS.

To evaluate the performance, models of converters and their control strategies were implemented. The grid models consisted of an ideal AC(DC) source with a resistance and an inductance. The SC model was

composed of a resistance in series with a capacitor, which represented SC performance. The IGCT model is the functional model in [40], which uses the PSIM package to treat the device as a "black box".

**Table.** Parameters of the multiterminal DC node.

| Converter | | Power/voltage | $R_f$or $R_c$ (m$\Omega$) | $L_f$ (mH) | $C_c$or $C_c'$ (mF) | Power (kW) |
|---|---|---|---|---|---|---|
| AC RTS $VSC_1$ | (AC) | 50 kVA/0.4 kV | 40.00 | 8.00 | | |
| AC RTS $VSC_1$ | (DC) | 50 kW/750 V | 0.25 | | 7.0 | 37.91* |
| AC SDN $VSC_2$ | (AC) | 50 kVA/0.4 kV | 40.00 | 8.00 | | |
| AC SDN $VSC_2$ | (DC) | 50 kW/750 V | 0.25 | | 7.0 | –21.02 |
| DC RTS $VSC_3$ | (AC) | 50 kVA/0.4 kV | 40.00 | 8.00 | | |
| DC RTS $VSC_3$ | (DC) | 50 kW/750 V | 0.25 | | 7.0 | –8.30 |
| PV DC-$DCC_1$ | (DC) | 50 kW/400 V | 2.00 | 0.25 | 1.2 | |
| PV DC-$DCC_1$ | (DC) | 50 kW/750 V | 0.25 | | 7.0 | 33.30 |
| SC DC-$DCC_2$ | (DC) | 50 kW/250-507 V | 20.0 | 4.00 | 5.0 | |
| SC DC-$DCC_2$ | (DC) | 50 kW/750 V | 0.25 | | 2.0 | –6.20 |
| Battery DC-$DCC_3$ | (DC) | 50 kW/168-236 V | 0.27 | 11.00 | 15.0 | |
| Battery DC-$DCC_3$ | (DC) | 50 kW/750 V | 0.25 | | 2.0 | –2.60 |
| V2G $VSC_4$ | (AC) | 50 kVA/0.4 kV | 40.00 | 24.00 | | |
| V2G $VSC_4$ | (DC) | 50 kW/750 V | 0.25 | | 5.0 | –29.73 |
| V2G DC-$DCC_4$ | (DC) | 50 kW/400 V | 15.0 | 3.00 | 5.0 | |
| V2G DC-$DCC_4$ | (DC) | 50 kW/750 V | 0.25 | | 5.0 | –3.36 |
| Cable | | $R_L$(m$\Omega$/m) | $L_L(mu$ H/m) | | $C_L(mu$ F/km) | |
| $L_1$ to $L_6$ | | 1.16 | 0.33 | | 0.5 | |
| $L_4'$, $L_5'$, $L_{6,}'L_{7,}L_8$ | | 0.154 | 0.27 | | 0.5 | |
| Length | | $L_1$ =10 m, $L_2$ =5 m, $L_3$ =10 m, $L_4$ =5 m, $L_4'$ =5 m, $L_5$ =5 m, $L_5'$ =10 m, $L_6$ =5 m, $L_6'$ =10 m, $L_7$ =2 m, $L_8$ =2 m | | | | |

The values of the RCD snubber unit in the $P_{CCF}$ protection were set according to [11] and the values of the clamp snubber unit were the same as in [32]. The HCB model was built in Simulink. Consequently, the interruption process was modelled by inserting arc models of MB [33,41]. The contact opening velocity was 8 m/s; the detection time of the logical circuit of MC was 60 $mu$ s; and the mechanical delay time of the electrodynamic drive was 180 $mu$ s [33]. The commutation time was approximately 70 $mu$ s, and the conduction time of the IGCT path was 100 $mu$ s. The tripping level of the $P_{CCF}$ protection was 10 kA, whereas the tripping levels for the $P_C$ protection were set at 2 kA and 375 V.

### 5.1. Protection system of the link DC bus and 0.4-kV AC SDN

Figure 10 shows the simulation results for the VSC of the 0.4-kV AC SDN in the case of a DC short-circuit fault with and without protection. The converter control monitors the AC and DC currents as well as the DC bus voltage to detect and localize DC faults. Therefore, when the variables exceed or fall below the thresholds and remain over/under them, the converter control detects the fault and turns off the converter switches (IGBTs) in about 2 $mu$ s. However, there are alternative current paths for the fault current, regardless of the state of the active switching devices within the converter.

Without any protection, the first wavefront occurred during the first phase (Figures 10a and 10c). The peak current and time to reach it were 344.02 p.u. (22.93 kA) and 0.205 ms, respectively. This large current discharging through the capacitor has the power to destroy it [14,42]. When $P_{CCF}$ protection was included, the

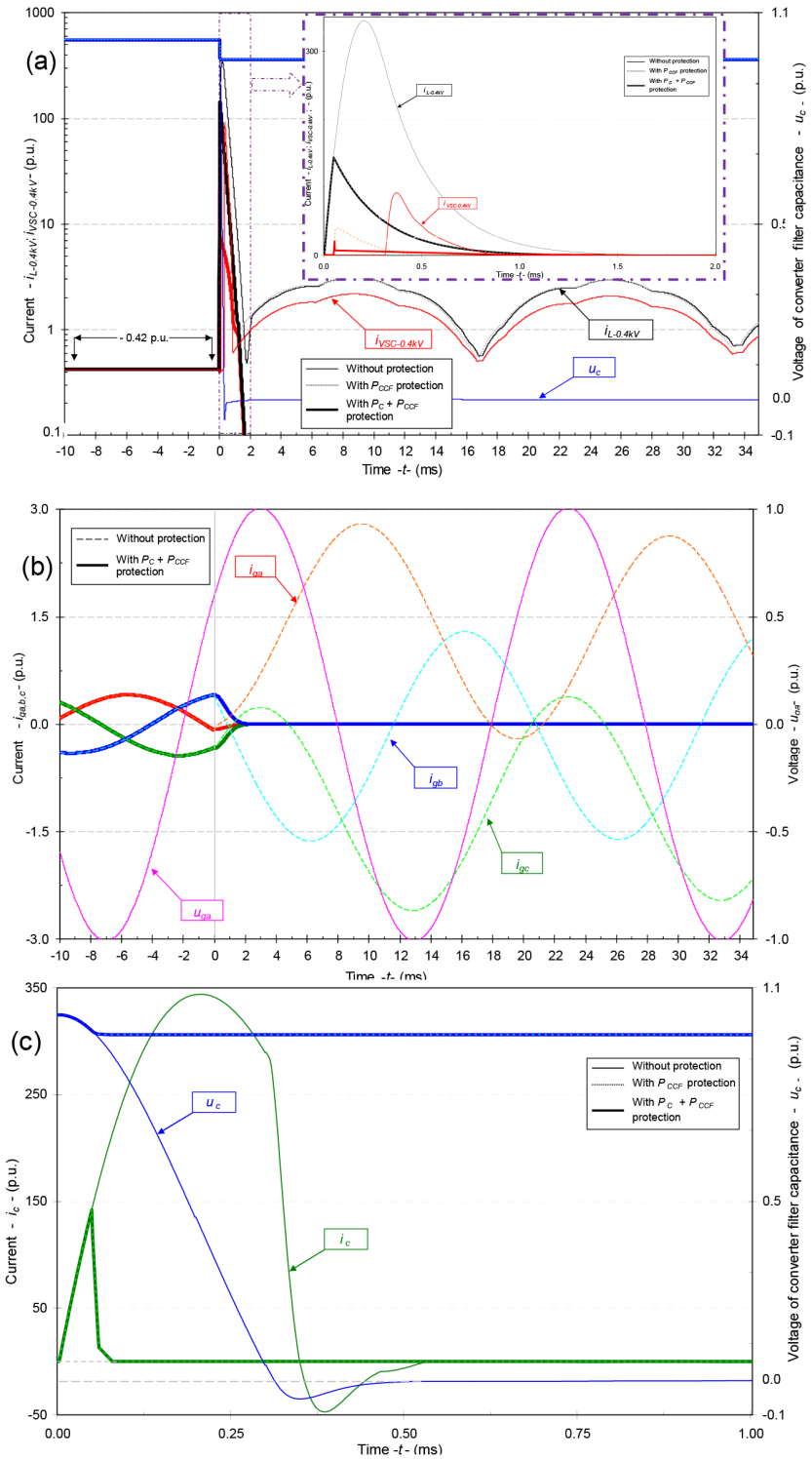


**Figure 10.** Three-phase VSC of the 0.4-kV AC SDN with a DC short-circuit fault with and without protection: a) $i_{L-0.4kV}$-cable inductor current; $i_{VSC-0.4kV}$-current provided by grid VSC; $u_c$-voltage and the current of converter filter capacitance; b) $i_{ga,b,c}$-grid-side three-phase current; $u_{ga}$-grid-side $a$ phase voltage; and c) $u_c$, $i_c$-voltage and current of the converter filter capacitance.

very rapid capacitor discharge crossed the 150-p.u. threshold limit (10 kA) of $P_{CCF}$ protection at 51 $mu$ s, and this interrupted the current in approximately less than 12 $mu$ s. The capacitor was thus satisfactorily protected. As shown, the voltage transient through the capacitor was suppressed by snubber circuits at a tolerable level. It is worth highlighting that the DC bus voltage decayed faster to zero when the capacitor was disconnected from the DC bus in anticipation of the freewheeling phase and the lower freewheeling current.

Without any protection, the most vulnerable components during the freewheeling phase are the freewheeling diodes, for which the current peak amplitude and the time interval to reach this peak were 92.08 p.u. (9.39 kA) and 0.369 ms, respectively (Figure 10a). This current spike damaged the diodes, which can handle a maximum current of 5 p.u. up to 10 ms. When $P_{CCF}$ protection was included, the current peak amplitude was limited to 39.11 p.u. (3.99 kA) and the time interval to reach this peak was 0.077 ms. At this point, $P_C$ protection was also included. With this condition, the fault current in the freewheeling path crossed the 19.59-p.u. threshold limit (2 kA) of $P_C$ protection at 54 $mu$ s, and this interrupted the current within 1.8 ms. The $P_C$ protection also blocked the grid-side current throughout the converter, which, without any protection, reached a 2.19-p.u. value (Figure 10b). This current value depends on the coupling reactors involved (equivalent Thevenin, transformer, grid filter, and the DC link line).

### 5.2. Protection system of the link DC bus and 25-kV AC RTS

Figure 11 shows the simulation results for the VSC of the 25-kV AC RTS in the case of a DC short-circuit fault with and without protection. Without any protection, the peak current in the first phase and the time interval to reach this peak were 215.89 p.u. (14.39 kA) and 0.274 ms, respectively. Furthermore, the peak current circulating through freewheeling diodes was 20.58 p.u. (1.81 kA) at 0.542 ms. When $P_{CCF}$ protection was applied, this interrupted the capacitor, which discharged at 0.144 ms. In addition, the performance of the $P_C$ protection interrupted the freewheeling path current at 1.96 ms. The freewheeling diodes were thus protected before they were damaged since the current reached 2.64 p.u at 8.12 ms without any protection.

The simulation results for a DC earth fault ( $R_f = 0$) are shown in Figure 12. This fault did not generate discharging current from the capacitor since it was unearthed. However, the peak current that circulated through the freewheeling diode current was 2.68 p.u. (0.473 kA) at 8.03 ms. Therefore, the $P_C$ protection should enable a 1.6-p.u. threshold limit (0.14 kA) for protection against this type of fault. This means that the freewheeling path current is interrupted at 4.70 ms.

### 5.3. Protection system of the link DC bus and 3-kV DC RTS

Figure 13 shows the simulation results for the VSC of the 3-kV DC RTS in the case of a DC short-circuit fault with and without $P_C$ protection. Without any protection, the peak current in the first phase and the time interval to reach this peak are 226.52 p.u. (15.09 kA) and 0.274 ms, respectively. When $P_{CCF}$ protection is applied, the capacitor discharge is interrupted at 0.137 ms. Since the configuration of the VSCs avoids the injection of 3-kV DC grid-side current into the dc fault, no $P_C$ protection is required.

### 5.4. Protection system of the link DC bus and battery bank

Figure 14 displays the simulation results for the DC-DCC of the battery bank in the case of a DC short-circuit fault with and without protections. Without any protection, during the first phase, the peak amplitude and the time interval to reach that peak were 218.74 p.u. (14.57 kA) and 0.118 ms, respectively. Moreover, the peak current that circulated through the freewheeling diode current was 67.13 p.u. (4.46 kA) at 0.176 ms. When

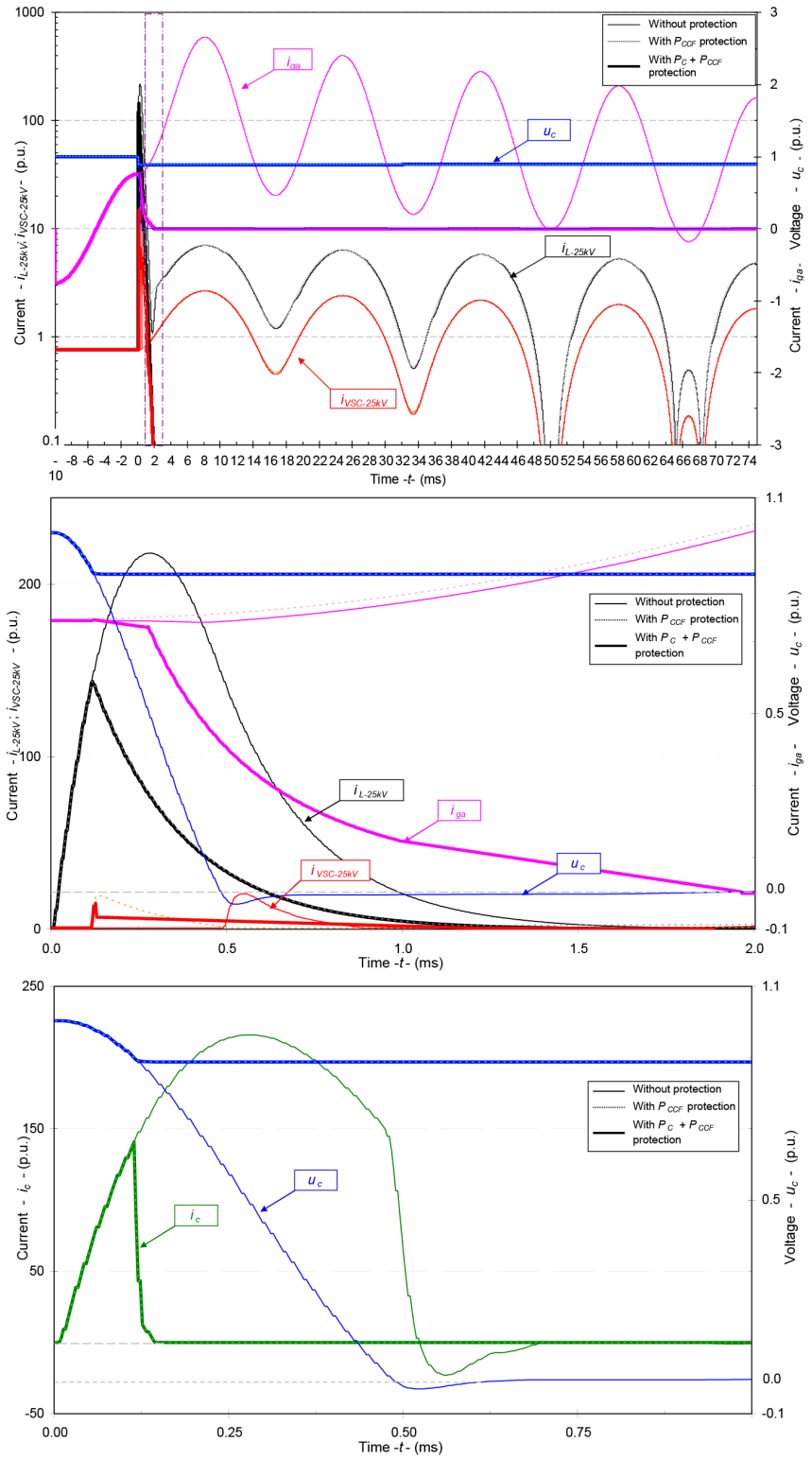


**Figure 11.** Single-phase VSC of the 25-kV AC RTS with a DC short-circuit fault with and without protection: $i_{L-25kV}$-inductor current; $i_{VSC-25kV}$-current provided by grid VSC; $u_c$, $i_c$-voltage and current of filter capacitance; $i_{ga}$-grid-side single-phase current.

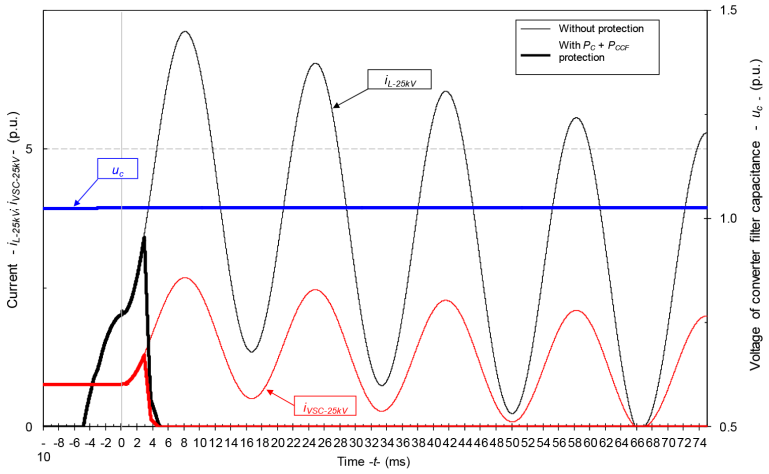


**Figure 12.** Single-phase VSC of the 25-kV AC RTS with a DC earth fault with and without protection: $i_{L-25kV}$-cable inductor current; $i_{VSC-25kV}$-current provided by grid VSC; $u_c$-voltage of converter filter capacitance.

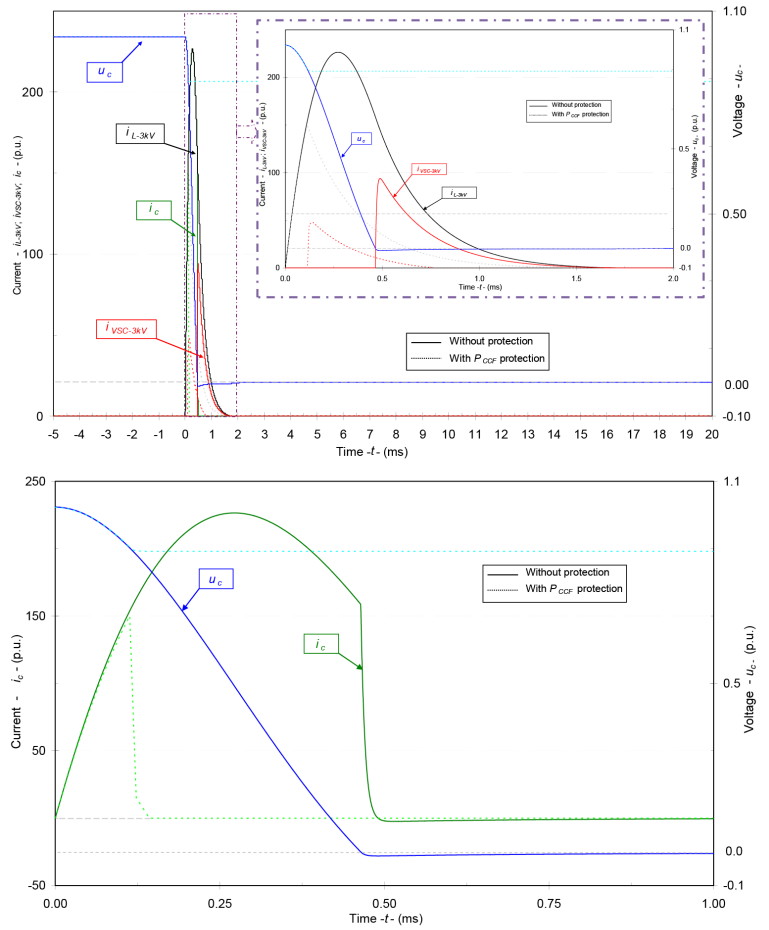


**Figure 13.** Three-phase VSC of the 3-kV DC RTS with a DC short-circuit fault with and without $P_C$ protection: $i_{L-3kV}$-cable inductor current; $i_{VSC-3kV}$-current provided by the grid VSC; $u_c$, $i_c$-voltage and current of the converter filter capacitance.

$P_{CCF}$ protection was applied, the capacitor discharge was interrupted at 0.071 ms. In addition, the freewheeling path current was interrupted at 1.91 ms. This protected the freewheeling diodes and the battery bank before they were damaged since the battery current reached 10.97 p.u (985.75 ms) without any protection. Battery voltage only experienced a 0.37% dip because of the performance of $P_C$ protection.

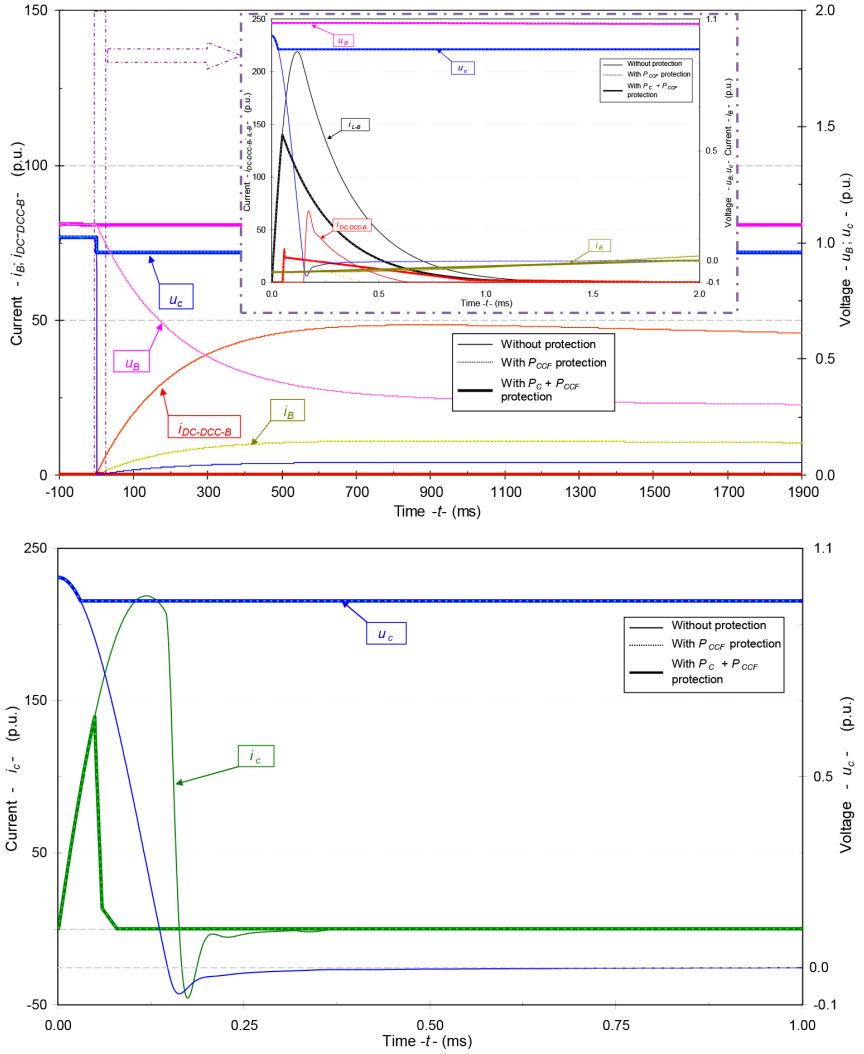


**Figure 14.** DC-DCC of the battery bank with a DC short-circuit fault with and without protection: $i_{L-B}$-cable inductor current; $i_{DC-DCC-B}$-current provided by the battery DC-DCC; $u_c$, $i_c$-voltage and current of the filter capacitance; $u_B$, $i_B$-battery voltage and current.

### 5.5. Protection system of the link DC bus and SC bank

When $P_{CCF}$ protection was applied to the SC bank, capacitor discharge was interrupted at 0.074 ms, thus effectively protecting the capacitor (Figure 15). In addition, thanks to the $P_C$ protection, the freewheeling path current was interrupted at 1.68 ms. In this way, freewheeling diodes and the SC bank were not damaged. SC voltage only experienced a 4.2% dip because of the redistribution of the stored inductive energy created during the fault condition just before the $P_C$ protection performance.

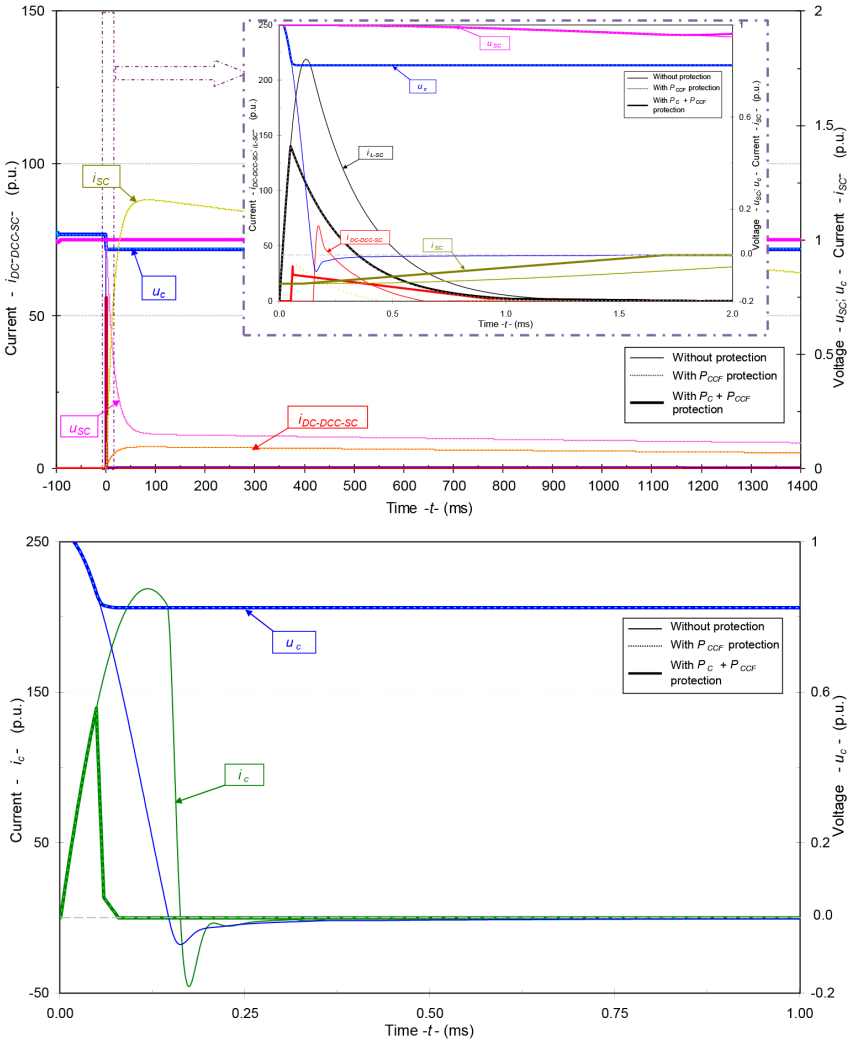


**Figure 15.** DC-DCC of the SC bank with a short-circuit fault with and without protection: $i_{L-SC}$-cable inductor current; $i_{DC-DCC-SC}$-current provided by the SC DC-DCC; $u_c$, $i_c$-voltage and current of the converter filter capacitance; $u_{SC}$, $i_{SC}$-SC voltage and current.

### 5.6. Protection system of all links in the DC bus

Figure 16 shows the simulation results of fault currents (with and without protections) for the majority of converters in the case of a DC short-circuit fault *F3*, i.e. at the input of DC-DCC$_4$. Without any protection, during the first phase, the respective large currents discharging through the capacitors have the power to destroy them. When $P_{CCF}$ protection was applied to all links, the capacitor discharges ($i_{ci}$) were interrupted appropriately. In addition, when $P_C$ protection was activated in all links, the freewheeling path currents and the converter-side currents ($i_{VSCi}$ or $i_{DC-DCDi}$) were also blocked properly.

The performance of several protections, at different time, could initiate an oscillatory voltage transient in the DC bus. However, as shown in Figure 16, the voltage transient of the DC bus maintains its value reduced, thanks to a shorter fault clearing time.

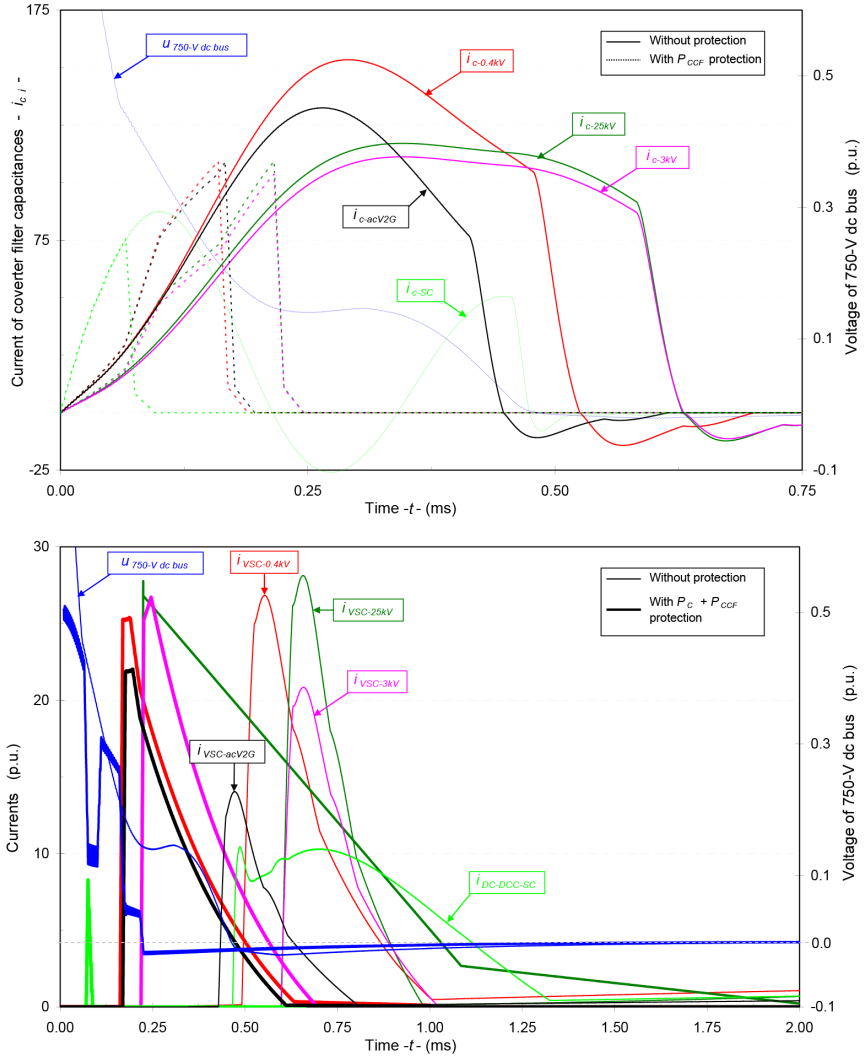


**Figure 16.** Converter currents with a short-circuit fault *F3* with and without protection.

## 6. Conclusion

This paper presented a multiterminal DC compact node capable of exchanging energy in a versatile, modular fashion among a 0.4-kV AC SDN, 25-kV AC RTS, 3-kV DC RTS, and a local DG system to feed EV charging stations. The foundations of this paradigm are the VSC and DC-DCC.

The outline and explanation of this new arrangement highlighted the challenges inherent in the protection of the DC compact node. This analysis quantified these challenges in terms of peak current magnitudes and the time interval necessary to reach that peak from the beginning of the fault. Based on the fault current profile, the paper proposed an optimal protection system design. This design is based on the use of SSCBs, HCBs, and protective relays, associated with converters, which monitor local quantities to detect and isolate DC faults as quickly as possible in order to prevent damage or destruction of the converters and filter capacitors of the node.

The simulation results of the actual multiterminal DC node illustrate that there are devices on the market that are capable of meeting the fast response requirements (around 10 *mu* s for capacitor protection and 2 ms for converter protection).

**Acknowledgments**

This work was carried out as part of the FerroSmartGrid Research Project: Railway Smart Grid, (ITC 20111044), which is funded by the Ministry of Science and Innovation in Spain. The project includes nine companies (Telvent Energía, Adif, Inabensa, Indra, Windinertia, Andel, Adevice, Telvent Transporte, and Acisa) and four universities (Seville, Malaga, Jaén, and Cordoba). The performance budget for this project was 9.6 million euros.

## References

[1] Haidar MA, Muttaqi KM, Sutanto D. Technical challenges for electric power industries due to grid-integrated electric vehicles in LV distributions: a review. Energ Convers Manage 2014; 86: 689-700.

[2] Falvo MC, Lamedica R, Bartoni R, Maranzano G. Energy management in metro-transit systems: an innovative proposal toward an integrated and sustainable urban mobility system including plug-in electric vehicles. Electr Pow Syst Res 2011; 81: 2127-2138.

[3] Motraghi A. Rail research projects: case studies. Res Trans E 2013; 41: 76-83.

[4] Steininger KW, Bachner G. Extending car-sharing to serve commuters: an implementation in Austria. Ecol Econ 2014; 101: 64-66.

[5] Sanchez-Sutil F, Hernandez JC, Tobajas C. Overview of electrical protection requirements for integration of a smart DC node with bidirectional electric vehicle charging stations into existing AC and DC railway grids. Electr Pow Syst Res 2015; 122: 104-118.

[6] Salomonsson D, Soder L, Sannino A. Protection of low-voltage DC microgrids. IEEE T Power Deliver 2009; 24: 1045-1053.

[7] Fletcher SDA, Norman PJ, Galloway SJ, Burt GM. Determination of protection system requirements for DC unmanned aerial vehicle electrical power networks for enhanced capability and survivability. IET Elect Syst Transport 2011; 1: 137-147.

[8] Cuzner RM, Venkataramanan G. The status of DC micro-grid protection. In: IEEE 2008 Industry Applications Society Annual Meeting; 5–9 October 2008; Edmonton, Alberta, Canada. New York, NY, USA: IEEE. pp. 1-8.

[9] International Electrotechnical Commission. Railway applications – Fixed installations – Electrical safety, earthing and the return circuit – Part 1: Protective provisions against electric shock. IEC 62128-1. Geneva, Switzerland: IEC, 2001.

[10] International Electrotechnical Commission. Railway applications – Fixed installations – Electrical safety, earthing and the return circuit – Part 2: Provisions against the effects of stray currents caused by DC traction systems. IEC 62128-2. Geneva, Switzerland: IEC, 2013.

[11] Mohan N, Undeland TM, Robbins WP. Power Electronics: Converter, Applications, and Design. 3rd ed. New York, NY, USA: Wiley, 2003.

[12] Liserre M, Dell'Aquila A, Blaabjerg F. An overview of three-phase voltage source active rectifiers interfacing the utility. In: IEEE 2003 Power Tech Conference; 23–26 June 2003; Bologna, Italy. New York, NY, USA: IEEE. pp. 1-8.

[13] Ottersten R, Svensson J. Vector current controlled VSC deadbeat control and saturation strategies. IEEE T Power Electr 2002; 17: 279-285.

[14] Baran ME, Mahajan NR. Overcurrent protection on voltage source converter-based multiterminal DC distribution systems. IEEE T Power Deliver 2007; 22: 406-412.

[15] Institute of Electrical and Electronics Engineers. Guide for the protection of stationary battery systems. IEEE 1375. New York, NY, USA: IEEE, 1998.

[16] Anderson PM. Power System Protection. New York, NY, USA: McGraw-Hill, 1999.

[17] Institute of Electrical and Electronics Engineers. Recommended practice for the design of DC auxiliary power systems for generating stations. IEEE 946. New York, NY, USA: IEEE, 2004.

[18] International Electrotechnical Commission. Short-circuit currents in DC auxiliary installations in power plants and substations – Part 1: Calculation of short-circuit currents. IEC 61660-1. Geneva, Switzerland: IEC, 1997.

[19] International Electrotechnical Commission. Short-circuit currents in DC auxiliary installations in power plants and substations – Part 3: Examples of calculations. IEC/TR 61660-3. Geneva, Switzerland: IEC, 2000.

[20] Yang J, Fletcher J, O'Reilly J. Multiterminal DC wind farm collection grid internal fault analysis and protection design. IEEE T Power Deliver 2010; 25: 2308-2318.

[21] Fletcher SDA, Norman PJ, Galloway SJ, Crolla P, Burt GM. Optimizing the roles of unit and non-unit protection methods within DC microgrids. IEEE T Smart Grid 2012; 3: 2079-2087.

[22] Nuutinen P, Peltoniemi P, Silventoinen P. Short-circuit protection in a converter-fed LV distribution network. IEEE T Power Electr 2013; 28: 1587-1597.

[23] Park JD, Candelaria J. Fault detection and isolation in low-voltage DC-bus microgrid system. IEEE T Power Deliver 2013; 28: 779-787.

[24] Fletcher SDA, Norman PJ, Fong K, Galloway SJ, Burt GM. High speed differential protection for smart DC distribution systems. IEEE T Smart Grid 2014; 5: 2610-2617.

[25] Barnes MJ, Blackmore E, Wait GD, Lemire-Elmore J, Rablah B, Leyh G, Nguyen MN, Pappas C. Analysis of high-power IGBT short circuit failures. IEEE T Plasma Sci 2005; 33: 1252-1261.

[26] Long HY, Luther-King N, Sweet MR, Narayanan EMS. Numerical evaluation of the short-circuit performance of 3.3-kV CIGBT in field-stop technology. IEEE T Power Electr 2012; 27: 2673-2679.

[27] Morton J. Circuit breaker and protection requirements for DC switchgear used in rapid transit systems. IEEE T Ind Appl 1985; IA-21: 1268-1273.

[28] Tang L, Ooi BT. Locating and isolating DC faults in multi-terminal DC systems. IEEE T Power Deliver 2007; 22: 1877-1884.

[29] Cinieri E, Fumi A, Salvatori V, Spalvieri C. A new high-speed relay protection of the 3-kV DC electric railway lines. IEEE T Power Deliver 2007; 22: 2262-2270.

[30] Krstic S, Wellner E, Bendre AR, Semenov B. Circuit breaker technologies for advanced ship power systems. In: IEEE 2007 Electric Ship Technologies Symposium; 21–23 May 2007; Hyatt Regency Crystal City, Arlington, Virginia, USA. New York, NY, USA: IEEE. pp. 201-208.

[31] Schmerda RF, Krstic S, Wellner EL, Bendre AR. IGCTs vs. IGBTs for circuit breakers in advanced ship electrical systems. In: IEEE 2009 Electric Ship Technologies Symposium; 20–22 April 2009; Baltimore, Maryland, USA. New York, NY, USA: IEEE. pp. 400-405.

[32] Alvarez S. Characterisation of 3.3 kV IGCTs for medium power applications. MSc, Polytechnic National Institute of Toulouse, Toulouse, France, 2005.

[33] Lund J. Assessment of switching technologies for application in HVDC-circuit breakers. MSc, Institute for HV Engineering, Stockholm, Sweden, 2011.

[34] Meyer JM, Rufer A. A DC hybrid circuit breaker with ultra-fast contact opening and IGCTs. IEEE T Power Deliver 2006; 21: 646-651.

[35] Henkilö- ja yritysarviointi SETI Oy. Low voltage electrical installations and safety at electrical work, National low voltage standard. Finnish SFS6000 Series. Helsinki, Finland.

[36] White RD. Railway electrification and protection. In: IET 2008 Professional Development course on Electric Traction Systems; 3–7 November 2008; Manchester, UK. New York, NY, USA: IEEE. pp. 258-305.

[37] Institute of Electrical and Electronics Engineers. Recommended practice for the design of DC auxiliary power systems for generating stations. IEEE 946. New York, NY, USA: IEEE, 2004.

[38] Hernandez JC, Vidal PG. Guidelines for protection against electric shock in PV generators. IEEE T Energy Conver 2009; 24: 274-282.

[39] Yang X, Choi MS, Lee SJ, Ten CW, Lim SI. Fault location for underground power cable using distributed parameter approach. IEEE T Power Syst 2008; 23: 1809-1816.

[40] Zhang'ao R, Kexun Y, Zhenxiu L, Caiyong Y, Yuan P. Design of a novel pulse capacitor charge power system based on inertial energy storage. In: IEEE 2009 International Conference on Power Electronics and Drive Systems; 2–5 November 2009; Taipei, Taiwan. New York, NY, USA: IEEE. pp. 1514-1517.

[41] Atmadji A. Direct current hybrid breakers: a design and its realization. MSc, Technical University of Eindhoven, Eindhoven, the Netherlands, 2001.

[42] Peuget R, Courtine S, Rognon JP. Fault detection and isolation on a PWM inverter by knowledge-based model. IEEE T Ind Appl 1998; 34: 1318-1326.